

Article

Controls on the Distribution of Invisible and Visible Gold in the Orogenic Gold Deposits of the Yangshan Gold Belt, West Qinling Orogen, China

Nan Li ¹, Jun Deng ^{1,*}, David I. Groves ^{1,2} and Ri Han ^{1,3,4,5}

¹ State Key Laboratory of Geological Processes and Mineral Resources, China University of Geosciences, Beijing 100083, China; sutoby@126.com (N.L.); di_groves@hotmail.com (D.I.G.); hanri@mail.iggcas.ac.cn (R.H.)

² Centre for Exploration Targeting, University of Western Australia, Crawley 6009 WA, Australia

³ Key Laboratory of Mineral Resources, Institute of Geology and Geophysics, Chinese Academy of Sciences, Beijing 100029, China

⁴ Institutions of Earth Science, Chinese Academy of Sciences, Beijing 100864, China

⁵ University of Chinese Academy of Sciences, Beijing 100049, China

* Correspondence: djun@cugb.edu.cn; Tel.: +86-(010)-82322301

Received: 11 December 2018; Accepted: 1 February 2019; Published: 4 February 2019



Abstract: Six orogenic gold deposits constitute the Yangshan gold belt in the West Qinling Orogen. Gold is mostly invisible in solid solution or in the sulfide lattice, with minor visible gold associated with stibnite and in quartz-calcite veins. Detailed textural and trace-element analysis of sulfides in terms of a newly-erected paragenetic sequence for these deposits, together with previously published data, demonstrate that early magmatic-hydrothermal pyrite in granitic dike host-rocks has much higher Au contents than diagenetic pyrite in metasedimentary host rocks, but lower contents of As, Au, and Cu than ore-stage pyrite. Combined with sulfur isotope data, replacement textures in the gold ores indicate that the auriferous ore-fluids post-dated the granitic dikes and were not magmatic-hydrothermal in origin. There is a strong correlation between the relative activities of S and As and their total abundances in the ore fluid and the siting of gold in the Yangshan gold ores. Mass balance calculations indicate that there is no necessity to invoke remobilization processes to explain the occurrence of gold in the ores. The only exception is the Py₁₋₂ replacement of Py_{1m}, where fluid-mediated coupled dissolution-precipitation reactions may have occurred to exchange Au between the two pyrite phases.

Keywords: invisible gold; visible gold; LA-ICP-MS; Yangshan gold belt; West Qinling

1. Introduction

Gold commonly has a complex distribution in gold deposits [1,2]. The gold that occurs in the structure of common sulfide minerals, or as discrete inclusions smaller than 100 nm, is referred to as ‘invisible gold’ [3]. Worldwide, pyrite and arsenopyrite are the most common hosts for invisible gold in gold deposits [4–6]. The other most common occurrence of gold is in the form of visible native gold, normally as distinct inclusions or filling fractures within these sulfide minerals [7–12], but also less commonly as nuggety gold in quartz veins. In orogenic gold systems, invisible gold within sulfides is normally followed by later visible gold [13–16]. Some authors have suggested that the visible native gold was remobilized from the invisible gold in sulfides [7,14,17–20], but it is unclear how gold could be first precipitated in pyrite and then become soluble in that pyrite, without transformation to pyrrhotite, and subsequently be re-precipitated from essentially the same ore fluid just a short distance away in the same ore zone [20]. In addition to this uncertainty, factors controlling the distribution of

invisible and visible gold are still unclear, with metamorphic grade; arsenic concentrations; and fluid temperature, pH, and oxidation or sulfidation state all interpreted to play important roles [14,21,22].

LA-ICP-MS is now a preferred technique for trace-element analysis of sulfides and other ore minerals, offering high sensitivities and an excellent spatial resolution [23–25]. Detailed interpretation of pyrite textures is critical in terms of interpreting their trace-element compositions [26–32]. Moreover, the correlation between the distribution of invisible/visible gold and the textures of sulfides and related ore assemblages has implications for defining ore paragenesis and the mechanisms of incorporation and/or release of invisible gold from the sulfides [24].

The West Qinling Orogen is the third largest gold province in China, with a total of >1100 t gold resources and >50 gold deposits [33,34]. Yangshan is a world-class gold belt in the southern part of the West Qinling Orogen and comprises six gold deposits, including the Anba (280 t gold), Getiaowan, Guanyinba, Gaoloushan, Nishan, and Zhangjiashan deposits. These deposits share many common features. They are all structurally-controlled, orogenic gold deposits [35] in metasedimentary rocks and granitic dikes, and have similar alteration mineralogies of quartz, sericite, and calcite and ore mineralogies of auriferous arsenian pyrite and arsenopyrite, with stibnite and visible gold. The paragenesis and geochemistry of ore minerals in the gold deposits of the Yangshan gold belt have been studied previously [36,37]. However, backscattered images (BSE) show that these previous studies ignored: (1) partial dissolution textures in the early pyrite; (2) the euhedral pyrite rims associated with the replacement of early pyrite cores by main ore-stage pyrite; and (3) the complex textures of two different pyrite generations within the main ore-stage pyrite, which can constrain the mechanisms of Au incorporation in, or release of Au from, the pyrite [17,24,32]. This study presents detailed textural and trace-element analysis of sulfides in terms of a newly erected paragenetic sequence, designed together with previously published data, to investigate the factors controlling the distribution of invisible and visible gold in the Yangshan ores to further improve genetic understanding of the deposits in the gold belt.

2. Geological Background

2.1. Regional Geology

The West Qinling Orogen is the western part of the Qinling Orogen Belt, which is viewed as the product of long-lived accretion and collision between the North China Craton, North Qinling Block, South Qinling Block, and South China Craton. The Kuanping, Shangdan, and Mianlue suture zones, respectively, separate the above continental blocks [38–41] (Figure 1).

Proterozoic metavolcanic-sedimentary formations (846–776 Ma), the oldest strata in the region, are located in the southeast of the West Qinling Orogen [42]. Cambrian, Silurian, Devonian, Carboniferous, Permian, Triassic, and Cretaceous strata are widespread, with Devonian and Triassic strata being important host rocks for gold mineralization (Figure 1) [43–45]. Mesozoic granitoids are widespread in the West Qinling Orogen (Figure 1). They mainly occur between the Shangdan and Mianlue suture zones or within the Mianlue suture zone and have zircon U-Pb ages of 245–185 Ma [46].

The Yangshan gold belt, along with other gold districts, is located in the Mianlue suture zone within the West Qinling Orogen and formed during post-collisional tectonism between the North and South China Craton (Figure 1) [37,47]. Large igneous intrusions are absent in the gold belt. The ~215 Ma Puziba dikes, comprising granite, aplite, and porphyry dikes, were sheared into lenses along the E-W-trending Anchanghe-Guanyinba Fault, which is a secondary fault of the Mianlue suture zone [46].

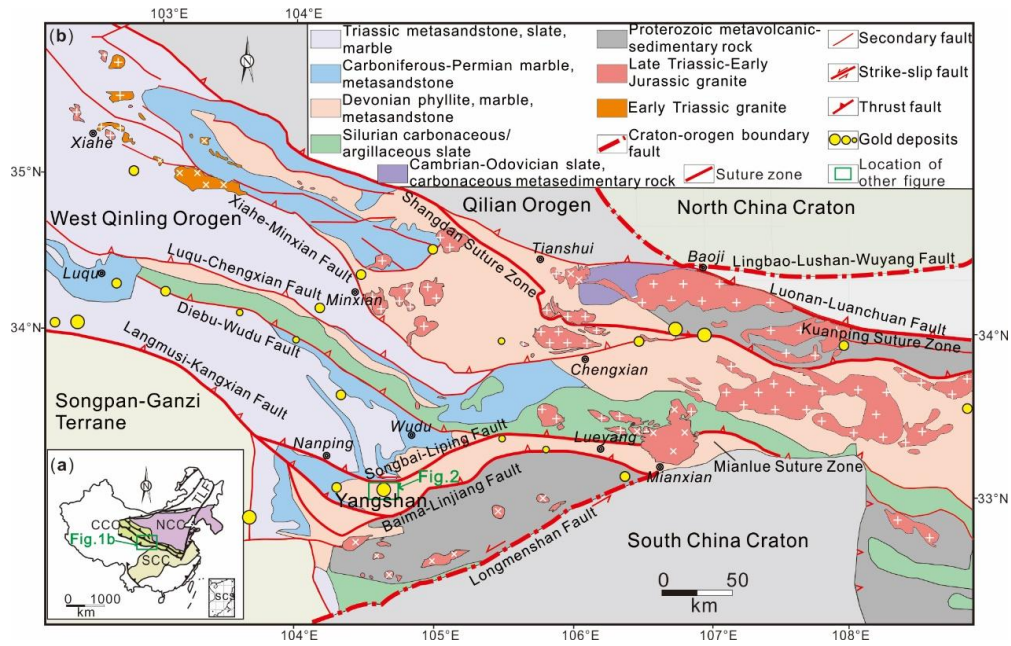


Figure 1. Simplified geological map of the West Qinling Orogen, showing the distribution of major crustal blocks, fault systems, and Mesozoic granitoids [47–49]. CCO, Central China Orogen; M, Mianlue; NCB, North China Block; SCB, South China Block; SCS, South China Sea; TLF, Tancheng–Lujiang Fault. (a): Tectonic overviews showing the position of West Qinling Orogen; (b): Schematic map showing the tectonic setting and distribution of gold deposits in West Qinling.

2.2. Deposit Geology

The deposits of the Yangshan gold belt are mainly hosted by Devonian phyllite and Triassic granitic dikes. Among the six gold deposits in the Yangshan gold belt, the Anba gold deposit hosts more than 90% of the gold resources in the district. However, all the deposits in the gold belt have similar geological and mineralogical characteristics [50,51].

Ore bodies in the gold belt are structurally controlled by the three splays (F1, F2, and F3) of the Anchanghe-Guanyinba Fault (Figure 2). Some of the ore bodies are also controlled by competency contrasts along contact zones between granitic dikes and phyllite (Figure 3a) [37].

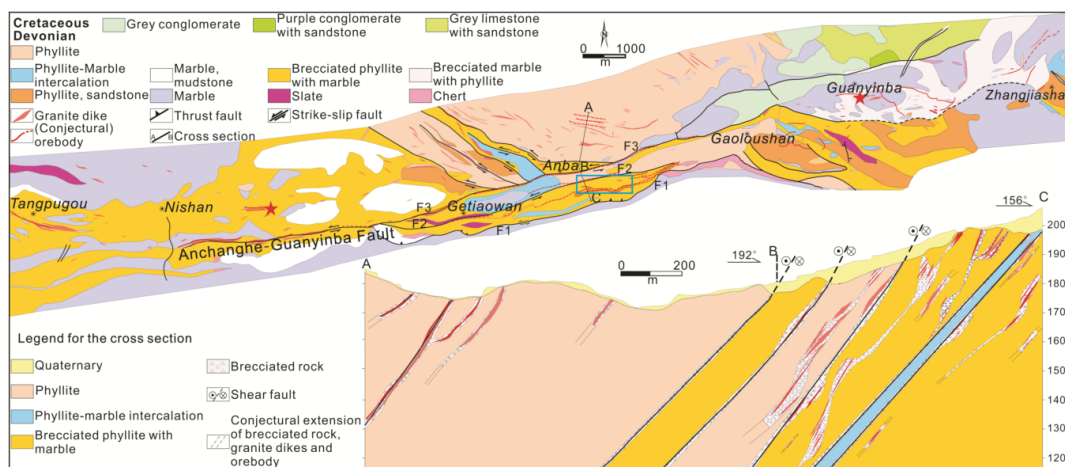


Figure 2. Geological map and cross-section of the Yangshan gold belt. Red stars and blue box are the sampling locations [37].

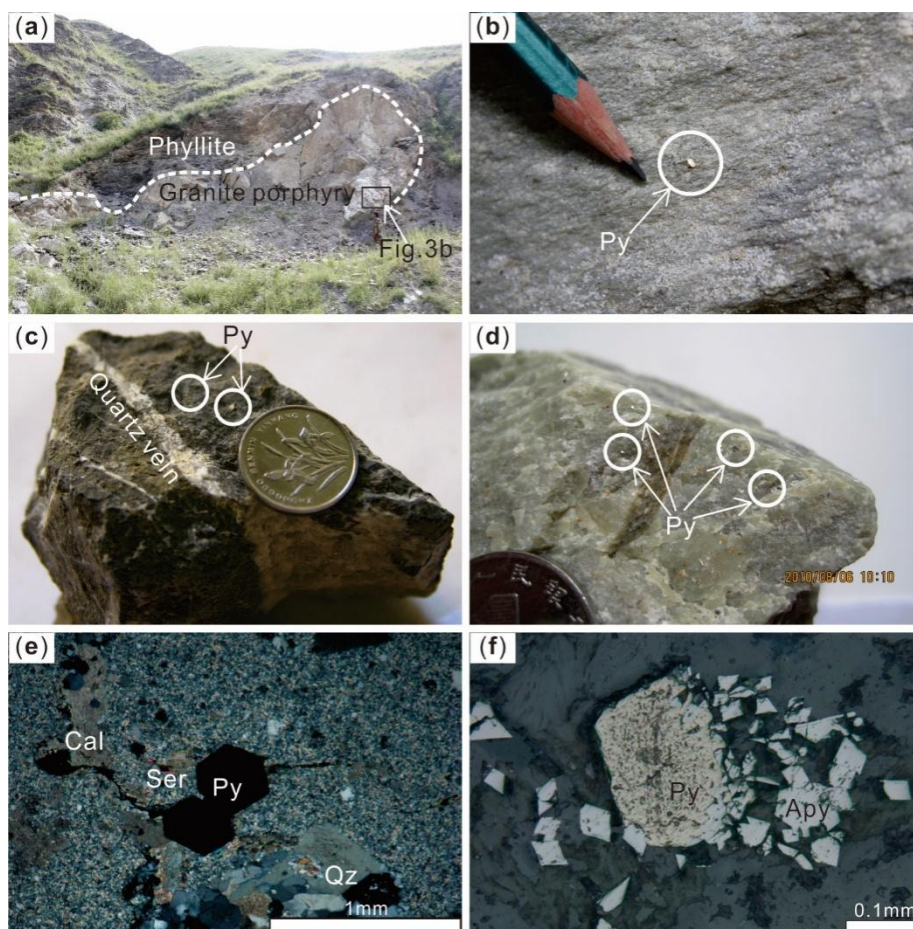


Figure 3. Ore styles and ore minerals from the Anba gold deposit. (a) The fault contact between granite porphyry dike and phyllite. (b) Pyrite is developed along the fault contact between granite porphyry and phyllite. (c) Pyrite in phyllite and quartz vein. (d) Pyrite in granite porphyry. (e) Silicification, sericitization, and pyrite mineralization in granite porphyry. (f) Arsenopyrite coexists with the outer rim of pyrite. Apy, arsenopyrite; Cal, calcite; Py, pyrite; Qz, quartz; Ser, sericite.

Major ore minerals in the gold belt include pyrite, arsenopyrite, and stibnite. Disseminated ores in phyllite or granitic dikes are the dominant ore type, with minor pyrite-arsenopyrite quartz veins, stibnite-bearing quartz veinlets, and quartz-calcite veins (Figure 3b–f) [36,37,52]. The diagenetic pyrite (Py_0) has a framboidal or colloform texture and is disseminated in the metasedimentary host rocks. Hydrothermal mineralization is divided into an early ore-stage (Py_1 –quartz), a main ore-stage (Py_2 – Apy_2 –quartz–sericite), and a late ore-stage (Py_3 – Apy_3 –stibnite–native gold–calcite–quartz). Pyrite is rare in the post-ore-stage quartz–calcite veins [37]. The alteration developed in the deposits is dominated by silicification, carbonation, sulfidation, and sericitization (Figure 3e). Gold is mostly invisible in solid solution or in the sulfide lattice, with minor visible gold associated with stibnite [36].

3. Analytical Techniques

Determination of mineral paragenesis was complemented by petrological work under transmitted and reflected light, and SEM. Based on careful examination of the mineral paragenesis, a suite of eight samples of pyrite from the granitic dikes (Table 1) was selected for LA-ICP-MS analyses at the U.S. Geological Survey, Denver, USA. Six samples are from the Anba gold deposit, and one sample each from the Guanyinba and Nishan gold deposits (Table 1), which are located to the east and west of Anba, respectively (Figure 2). These three deposits are considered representative of the Yangshan gold belt. Grey-green equigranular to porphyritic granitic dikes include granite, plagioclase granite,

granite porphyry, and plagioclase granite porphyry, which are common to all three deposits. The primary minerals in the dikes are plagioclase, quartz, and biotite, which are commonly altered to sericite, chlorite, epidote, and clays.

Table 1. Descriptions of the samples analysed in this study. Samples listed in a hierarchical manner under Deposit and then Sample Number.

Deposit	Sample Number	Lithology	Pyrite Stage
Anba	AB10PD4-102	Granite porphyry dike with quartz-calcite vein	Py _{1m}
Anba	AB10PB4-108_2	Granite porphyry dike with quartz vein	Py _{2a} , Py _{2b}
Anba	SM1-3	Granite	Py _{1m} , Py ₁₋₂ , Py _{2a} , Py _{2b}
Anba	YS-AB-10-PD1-01	Plagioclase granite dike with quartz-calcite veins	Py _{1m} , Py _{2b}
Anba	YS-AB-10-PD1-03	Granite dike in fault zone with quartz vein	Py _{1m} , Py ₁₋₂ , Py _{2a} , Py _{2b}
Anba	YS-AB-10-PD1-04	Plagioclase granite porphyry dike with quartz vein	Py _{1m} , Py _{2b}
Guanyinba	ZK054-4	Granite	Py _{2a} , Py _{2b}
Nishan	YS-NS-10-05	Plagioclase granite porphyry dike	Py _{2b}

The LA-ICP-MS analyses on pyrite were conducted on a Photon Machines Analyte G2 193 nm laser ablation system attached to a Perkin Elmer ELAN DRC-e ICP-MS. Laser ablation ICP-MS methods for pyrite are based on [26,53]. Both 15- and 30-micron diameter laser spots were used for the analyses. A laser fluence of 2 J/cm² and frequency of 5 Hz were used for the analyzed spots. Helium was used as a carrier gas. Calibration was conducted using the USGS MASS-1 sulfide reference material run five to ten times at the beginning of each session, following the procedures of [54] and using Fe as the internal standard element [26]. Concentration calculations were carried out using off-line data processing following the equations of [54]. The MASS-1 reference material was run periodically to monitor for drift. During these analytical sessions, drift was less than five percent for all elements. A stoichiometric value of 46% Fe was used for the LA-ICP-MS concentration calculations. Detection limits were calculated as three times the standard deviation of the blank [54] and are shown in Table S1. Data were examined for the presence of mineral inclusions or zoning recorded in the time resolved spectra as deviations from a stable signal (e.g., [26,53]). Because some data are below the detection limits of the analytical techniques, corrections are necessary for the incorporation into the statistical method. Data qualified with a “less than” value were replaced with 0.7 times the detection limit.

4. Textures of Pyrite and Mineral Paragenesis

Core-rim zonation is common in pyrite from deposits in the Yangshan gold belt, with the earlier-formed Py₀ and Py₁ as the core, and the main ore-stage Py₂ as the rim of the pyrite [36,37]. In this study, a more detailed analysis of pyrite textures improves paragenetic understanding of the deposits from the Yangshan gold belt.

4.1. Partial Dissolution Textures of Py_{1m}

To distinguish different Py₁ cores, the Py₁ hosted by the granitic dikes is named Py_{1m} and Py₁ from metasedimentary rocks is named Py_{1s}. Besides the normal core-rim texture formed by Py_{1m} and Py₂, the partial dissolution texture of Py_{1m} is recognized in this study. The inner Py_{1m} core has been partially replaced and overgrown by a Py₂ rim and formed a new pyrite generation (Py₁₋₂), which has a brighter response in BSE images than Py_{1m} and is therefore distinguishable from Py_{1m} and Py₂ in such images. Furthermore, Py₁₋₂ retains the shape of Py_{1m} through pseudomorphic replacement (Figure 4a–h).

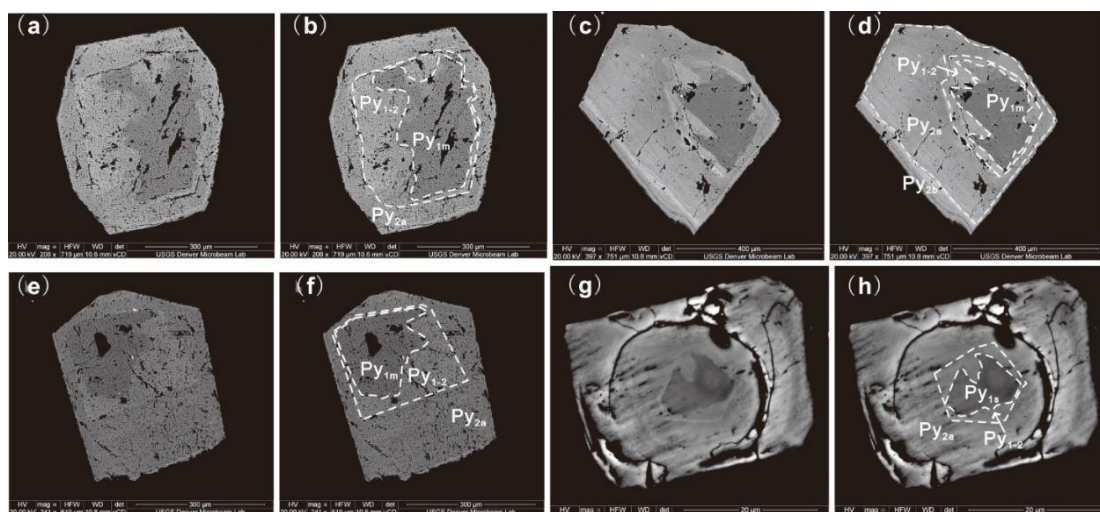


Figure 4. BSE images showing the pseudomorphous replacement textures of Py_1 and Py_2 . (a,b): Sample number SM1-3-2; (c,d): Sample number SM1-3-3; (e,f): Sample number SM1-3-4; (g,h): Sample number SM4-2-25-2.

4.2. Complex Textures within Py_2

Within the traditional main ore-stage Py_2 , an irregular bright pyrite band (a few micrometres wide) with As enrichment is recognized in BSE images. The pyrite within the bright band is named Py_{2a} and the pyrite exterior to it is named Py_{2b} (Figure 4c,d; Figure 5a–h). Fine-grained arsenopyrite is located around the bright band, whereas relatively coarse-grained prismatic arsenopyrite is paragenetically associated with Py_{2b} (Figure 5a–h).

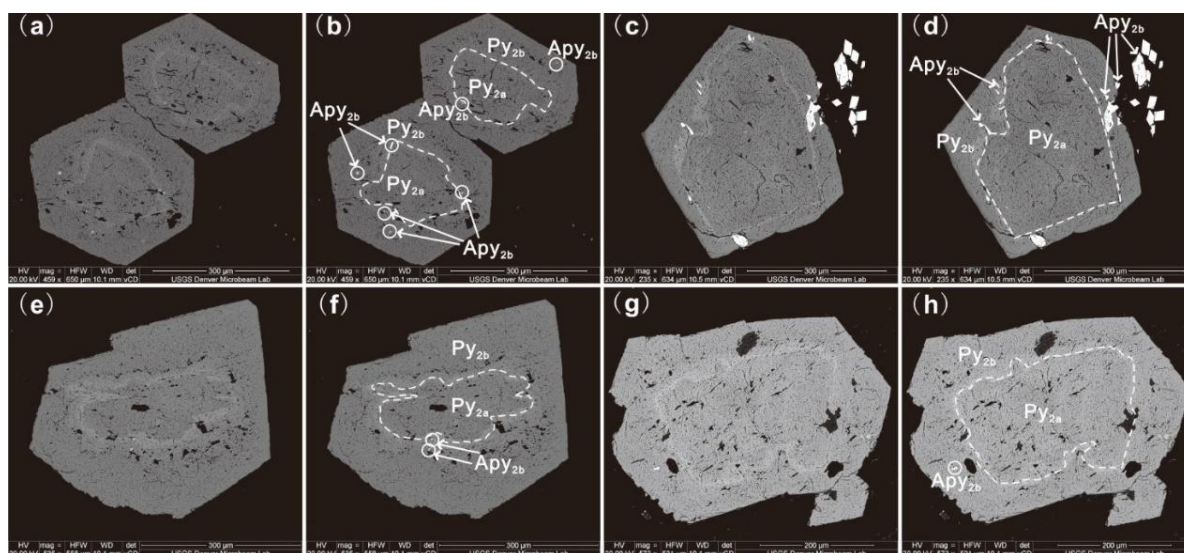


Figure 5. BSE images showing the bright band and replacement textures of Py_{2a} and Py_{2b} . (a,b): Sample number AB10PD4-108(2)-5; (c,d): Sample number YS-AB-10-PD1-03-4; (e,f): Sample number AB10PD4-108(2)-11; (g,h): Sample number AB10PD4-108(2)-12.

4.3. Mineral Paragenesis

Recognition of the pseudomorphic replacement texture between Py_1 and Py_2 , and the bright band with arsenopyrite enrichment within Py_2 , leads to the improvement of the paragenetic sequence diagram of the Yangshan gold belt (Figure 6). The multiple generations of pyrite from early diagenesis through the peak- to post- ore-stage, as well as trace-element evolution of the sulfides during the

pre- to main- ore-stage described below, indicate more complicated ore-forming processes than were previously supposed to exist in the Yangshan gold belt.

Minerals	Diagenetic Stage	Pre-Ore Stage	Main Ore Stage	Late Ore Stage	Post Ore Stage
Pyrite	<u>Py₀</u>	Py _{1m} /Py _{1s}	Py _{2a} Py _{2b}	Py ₃	Py ₄
Arsenopyrite			Py ₁₋₂ Apy _{2b}		
Gold		Invisible gold	Invisible gold	Visible gold	
Stibnite					
Sphalerite					
Galena					
Chalcopyrite					
Sulfosalt minerals					
Quartz					
Calcite					
Sericite					
Kaolinite, Montmorillonite					

Figure 6. Paragenetic sequence of gold mineralization and alteration of the gold deposits of the Yangshan gold belt. The bold lines indicate high abundance, the thin lines represent the minor amounts, and the discontinuous lines indicate uncertainty in the determination of the paragenetic sequence due to the lack of a clear textural relationship [35].

5. Trace Element Compositions of Pyrite and Arsenopyrite

As there is only minor pyrite in the diagenetic, late-, and post-ore stages, and their geochemistry is summarized by [36], the geochemistry of newly recognized Py_{1m}, Py₁₋₂, Py_{2a}, and Py_{2b} from the pre- and main-ore stage mineralization is emphasized in this paper (Table 1). A total of 119 LA-ICP-MS spot analyses were completed on various pyrite generations from Yangshan. A total of nine elements were analysed and interpreted in this study: Ag, As, Au, Bi, Co, Cu, Ni, Pb, and Sb. The pyrite results, together with Apy_{2b} and stibnite data from [37], are given in Table S1 and elemental variation is presented in Figure 7. Representative pyrite textures and geochemistry within single pyrite grains are shown in Figures 8 and 9.

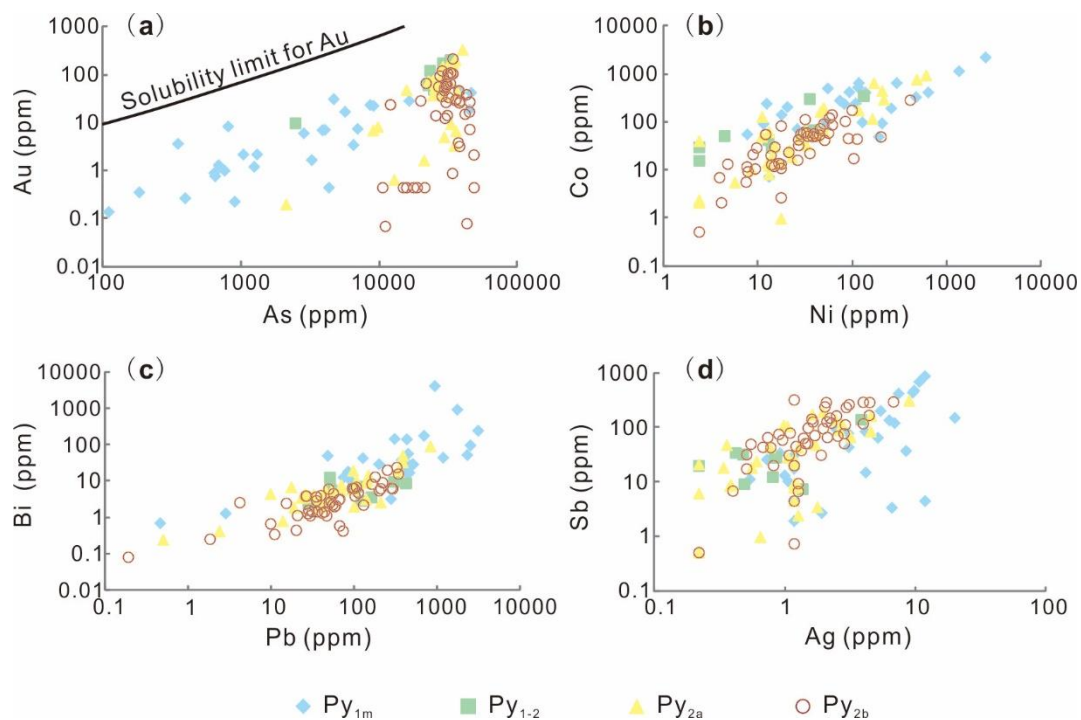


Figure 7. Trace-element binary plots of Au against (a) As, (b) Ni, (c) Pb, and (d) Ag for Yangshan pyrites. The line in (a) is the inferred solubility limit of gold in arsenian pyrite [21]. The trace-element concentrations are from Table S1, or calculated using 0.7 times mdl (minimum detection limit) values for all measurements <mdl.

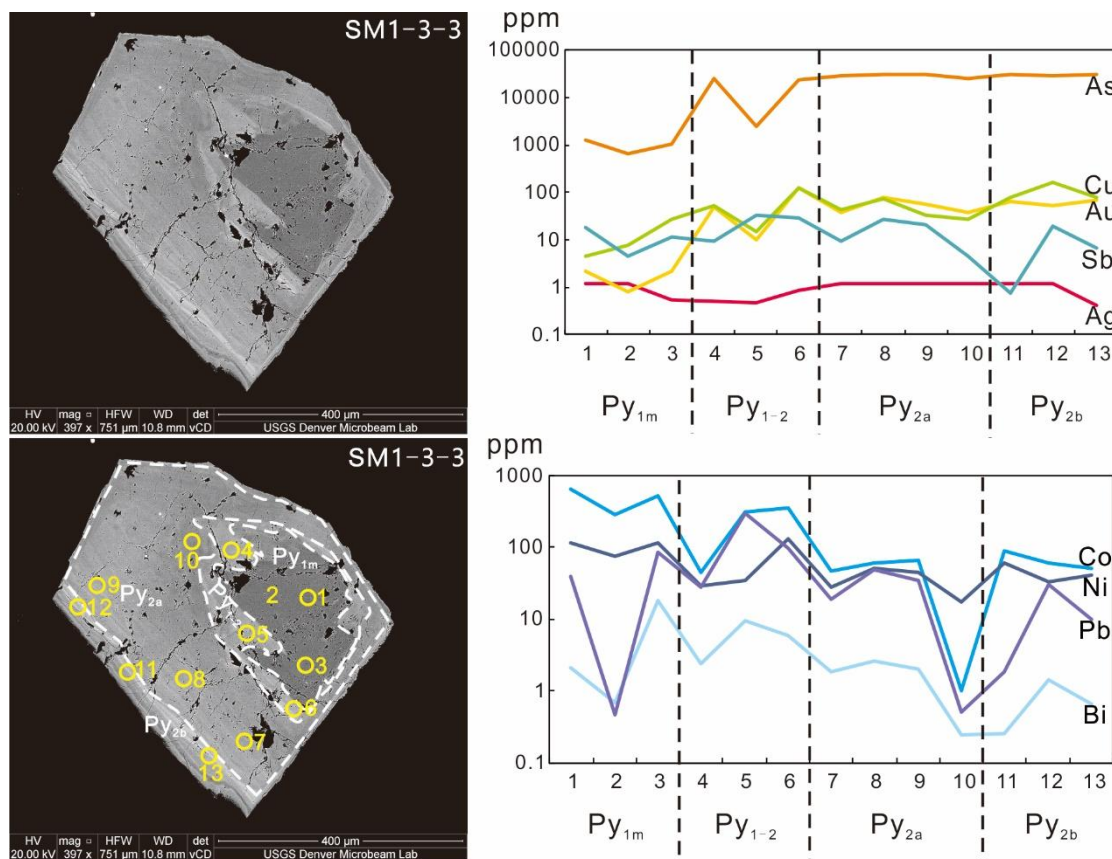


Figure 8. The core-rim texture of pyrite in sample SM1-3-3 and the trace-element contents analysed by LA-ICP-MS within each zone.

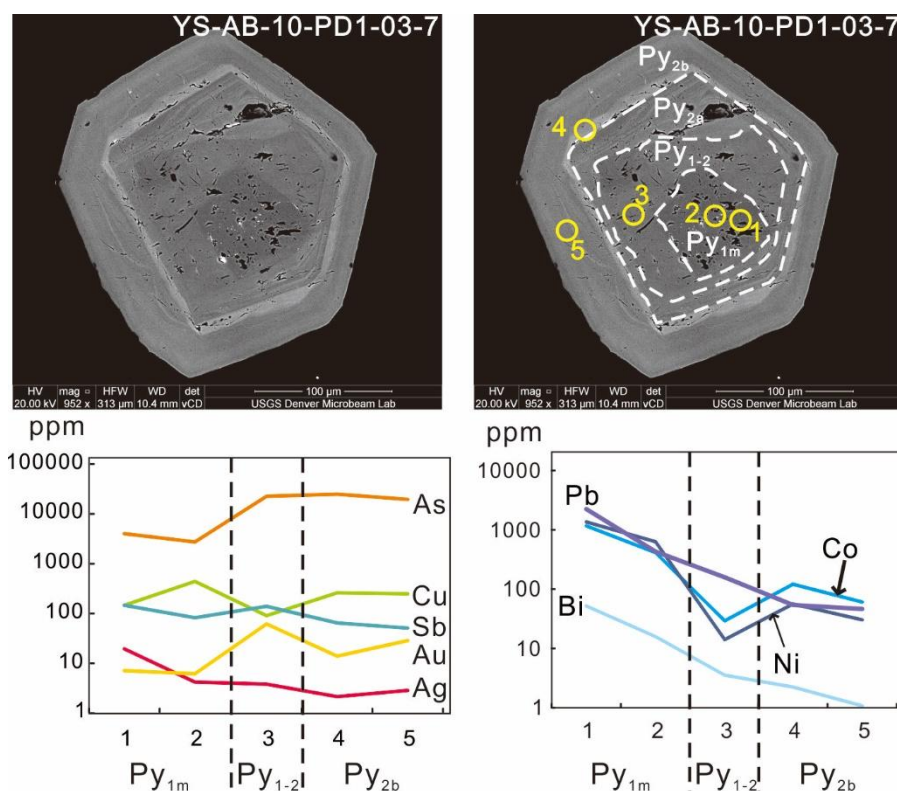


Figure 9. The core-rim texture of pyrite in sample YS-AB-10-PD1-03-7 and the trace-element contents analysed by LA-ICP-MS within each zone.

The median As contents in Py_{1m} , Py_{1-2} , Py_{2a} , and Py_{2b} are 3221, 28672, 28583, and 30,868 ppm, with ranges of 109–45803, 2454–32613, 2103–39768, and 10501–48107 ppm, respectively. The median Au contents in Py_{1m} , Py_{1-2} , Py_{2a} , and Py_{2b} are 3.7, 71, 56, and 28.2 ppm, with ranges of <0.39–54, 9.88–207, 0.2–337, and <0.64–123 ppm, respectively (Table S1). Although there is considerable variation, the As and Au contents in Py_{1-2} , Py_{2a} , and Py_{2b} are higher than Py_{1m} (Figures 7a and 10; Table S1), as also shown by the As and Au contents of single pyrite grains (Figures 8 and 9). Py_{1-2} has the highest Au content compared with Py_{1m} , Py_{2a} , and Py_{2b} (Figures 9 and 10). There is a decreasing trend of Au contents from Py_{1-2} , through Py_{2a} , to Py_{2b} (Figure 10; Table S1). Py_{2b} has the highest As, Cu (median 347 ppm), and Sb (median 67.5 ppm) contents compared to Py_{1m} , Py_{1-2} , and Py_{2a} (Figure 10; Table S1).

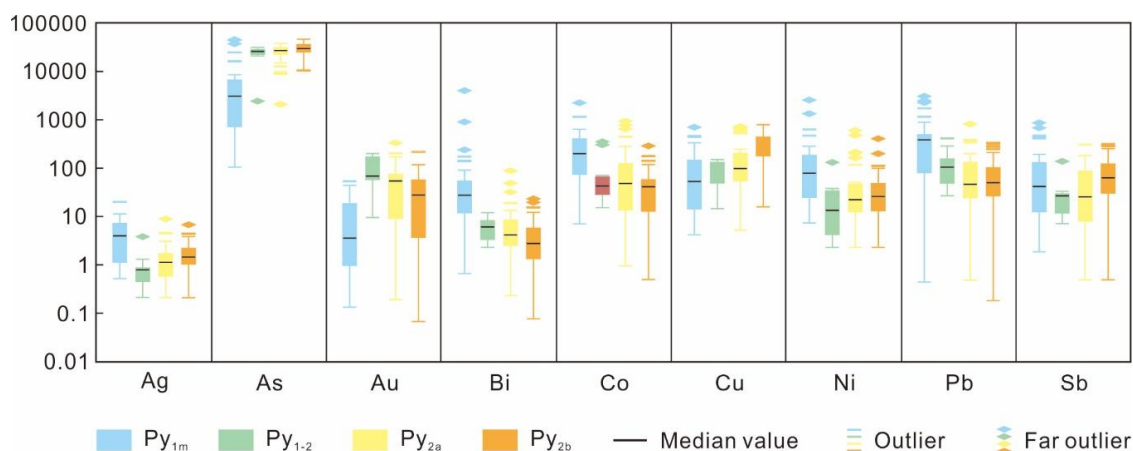


Figure 10. Box plot of trace-element concentrations of Yangshan pyrite. Boxes represent interquartile range (data between 25th and 75th percentiles), with top and bottom lines extending 1.5 times the interquartile range toward the maximum and minimum, respectively.

The median Cu contents in Py_{1m}, Py₁₋₂, Py_{2a}, and Py_{2b} are 55.2, 91.8, 103, and 347 ppm, with ranges of <13.9–708, 15.2–159, 5.43–730, and 16.5–826 ppm, respectively (Table S1). Generally, Cu contents increase from early Py_{1m}, through Py₁₋₂ and Py_{2a}, to Py_{2b}.

The median Pb contents in Py_{1m}, Py₁₋₂, Py_{2a}, and Py_{2b} are 401, 108, 48.4, and 53.4 ppm, with ranges of 0.46–3089, 28–418, 0.5–825, <0.27–338 ppm, respectively (Table S1). The median Bi contents in Py_{1m}, Py₁₋₂, Py_{2a}, and Py_{2b} are 28.6, 6.3, 4.3, and 3 ppm, with ranges of <0.98–4052, 2.41–12.4, 0.24–89.1, and <0.11–23.4 ppm, respectively (Table S1). Lead and Bi contents decrease from Py_{1m}, through Py₁₋₂ and Py_{2a}, to Py_{2b}.

The median Co contents in Py_{1m}, Py₁₋₂, Py_{2a}, and Py_{2b} are 209, 44.3, 50.2, and 44 ppm, with ranges of 7.32–2262, 15.8–354, 0.99–947, and 2.11–291 ppm, respectively. The median Ni contents in Py_{1m}, Py₁₋₂, Py_{2a}, and Py_{2b} are 82.1, 14, 23.1, and 27.7 ppm, with ranges of <18.8–2582, <3.41–133, <3.41–606, and <3.41–410 ppm, respectively (Table S1). Cobalt and Ni contents broadly parallel Pb and Bi, but there is lower Co and Ni in Py₁₋₂ (Figures 7 and 10; Table S1).

The Au-As correlation becomes weaker from early Py_{1m}, through Py₁₋₂ and Py_{2a}, to Py_{2b} (Table S2). For Py₁₋₂, there is a strong positive correlation between Au and Cu, which is unique among all pyrite stages (Table S2). Cobalt and Ni contents show a positive correlation among all pyrite generations (Figure 7b; Table S2). Lead and Bi in Py_{2a} and Py_{2b} have a strong positive correlation compared with that of the same elements in Py₁ and Py₁₋₂ (Figure 7c; Table S2).

As summarized in [37], the Au content of Apy_{2b} ranges from <0.046 to 1205 ppm (median 15.4 ppm, average 143 ppm), whereas the Au content of late ore-stage stibnite ranges from 0.02 to 0.42 ppm (median 0.08 ppm, average 0.12 ppm).

6. Discussion

6.1. Invisible and Visible Gold in the Gold Ores

Py_{1m} within granitic dike host-rocks has a low Au content (<0.39~54 ppm, median 3.7 ppm), which is lower than the Au values in later generations of pyrite, but is higher than the gold values in diagenetic pyrite in phyllite (median 0.32 ppm; [37]). The $\delta^{34}\text{S}$ values of pyrite cores (Py_{1m} in this study) in granitic dikes from the Yangshan gold belt have a very limited range from 0 to 1.3‰, consistent with a magmatic-hydrothermal origin [55]. Similar magmatic-hydrothermal pyrite from the Wallaby gold deposit in Western Australia has median gold values of 0.35 ppm, with individual spot data as high as 78 ppm [56]. LA-ICP-MS analysis also shows that gold contents range from <0.03 to 2.1 ppm in the magmatic-hydrothermal cores of pyrites in syenite from the Chang'an gold deposit, China [57].

The magmatic-hydrothermal Py_{1m} has lower contents of As, Au, and Cu than ore-stage pyrite, but the values are higher than the As, Au, and Cu contents in other magmatic-hydrothermal pyrites described by [56,57]. The contrast in element patterns between Py_{1m} and ore-stage pyrites, combined with their erratic, more negative $\delta^{34}\text{S}$ values [50,58], indicate that the auriferous ore-fluids were not magmatic-hydrothermal in origin. Considering the sharp contact between Py_{1m} and Py₁₋₂, and the low metamorphic grade in the region, the replacement textures clearly shown by Py₁₋₂ raise the possibility that the enhanced Au values of Py_{1m} resulted from fluid-mediated coupled dissolution-precipitation reactions [17,20,24,32,59,60].

According to the flotation test report, the contents of pyrite, arsenopyrite, and stibnite in the primary ores are 2.02%, 0.93%, and 0.18%, respectively [61]. Based on observations under the microscope, the contents of Py₀, Py_{1s}, Py_{1m}, Py₁₋₂, Py_{2a}, Py_{2b}, Apy_{2b}, and stibnite in the ores are estimated to be 0.005%, 0.005%, 0.005%, 0.005%, 1.5%, 0.5%, 0.93%, and 0.18%, respectively. Using the average gold contents of pyrite, arsenopyrite, and stibnite from each ore stage (0.26 ppm, 0.82 ppm, 11.81 ppm, 105.98 ppm, 70.05 ppm, 36.91 ppm, 143 ppm, 0.12 ppm, for Py₀, Py_{1s}, Py_{1m}, Py₁₋₂, Py_{2a}, Py_{2b}, Apy_{2b}, and stibnite, respectively; Table S1) [37], the invisible gold contained in sulfide in one tonne of ore is calculated to be 1.3×10^{-5} g, 5.9×10^{-4} g, 4.1×10^{-5} g, 5.3×10^{-3} g, 1.05 g, 0.18 g,

1.33 g, and 2.2×10^{-4} g for Py₀, Py_{1s}, Py_{1m}, Py₁₋₂, Py_{2a}, Py_{2b}, Apy_{2b}, and stibnite, respectively. Clearly, Py_{2a}, Py_{2b}, and Apy_{2b} are the only significant contributors to the gold budget. The total invisible gold locked in the structures of pyrite, arsenopyrite, and stibnite in one tonne of ore is 2.57 g. As 83.73% of gold is located in sulfides with 16.27% as visible gold that is enclosed in other minerals [61], there is 0.50 g native gold in one tonne of ore. Therefore, there is a calculated 3.07 g gold in one tonne of ore. The calculated gold grade is lower than the reported average gold grade (4.76 g/t) [62], which may be caused by the limited number of arsenopyrite samples in this study. In previous studies of Yangshan gold deposits, arsenopyrite has been shown to have Au contents as high as 4719 ppm (average 2073 ppm) [63]. This average is about 15 times greater than that of this study. Using the average Au content in [63] would add 18 g Au to the total gold budget, which would clearly exceed the known gold grade. The true Au content of arsenopyrite must lie between that of [63] and this study, but closer to this study.

6.2. Controls on the Distribution of Invisible and Visible Gold

The replacement of Au-As-poor Py₁ by Au-As-rich Py₂ and the formation of As-Au-rich Py₁₋₂ indicate that the pre-ore magmatic-hydrothermal Py_{1m} became unstable and was partially replaced during ingress of the auriferous ore fluid, with Py₁₋₂ rimming the Py_{1m} cores and tending to form crystal shapes. No arsenopyrite was developed in this stage to compete with pyrite for Au distribution, leading to the high Au concentrations in Py₁₋₂, which was then overgrown by Py_{2a, b}.

The bright pyrite band between Py_{2a} and Py_{2b} in BSE images, which is the reaction front of replacement [17], has a high As content (Figure 8), indicating that the ore fluid evolved to be As-rich during the late main-ore stage. Py_{2b} has the highest As content, but the lowest Au content, of all main ore-stage pyrites, consistent with its very low Au-As correlation coefficient (Table S2). This is due to the fact that Au preferentially entered the lattice of arsenopyrite that was intimately intergrown with Py_{2b}, as also shown by [51]. Py_{2b} contains more Sb than Py_{1m}, Py₁₋₂, and Py_{2a}, which indicates Sb enrichment during the late main ore-stage. Once stibnite formed in the absence of pyrite or arsenopyrite, there was no suitable host for invisible gold and free gold was deposited in cracks or on grain surfaces of the earlier-formed sulfides, as also described by [36,37].

The physicochemical parameters of ore formation in the Yangshan gold belt are estimated as follows. Based on the micro-thermometry of primary fluid inclusion, the mineralization temperatures of the main ore-stage and late ore-stage were 288–300 °C, and 271–288 °C, respectively [51,52]. The sulfur fugacity during the main ore-stage at the Yangshan gold belt can be estimated to have been $10^{-10.3} \sim 10^{-11.1}$, which is similar to the calculated sulfur fugacity ($10^{-10.4}$) based on the As contents in arsenopyrite [51]. The sulfur fugacity during the late ore-stage is estimated to have been $10^{-13.5} \sim 10^{-11.1}$ (Figure 11). Temperature and sulfur fugacity are two important factors controlling the stability of stibnite [64,65]. During the main ore-stage, pyrite and arsenopyrite precipitated at temperatures between 288 and 300 °C, and the majority of gold occurred within the lattices of pyrite and arsenopyrite. The precipitation of pyrite and arsenopyrite reduced the concentration of available reduced sulfur in the ore fluid. During the late ore-stage, the temperature decreased to 271–288 °C and the sulfur fugacity to $10^{-13.5} \sim 10^{-11.1}$, leading to the decrease of antimony solubility and precipitation of stibnite and native gold [64,66].

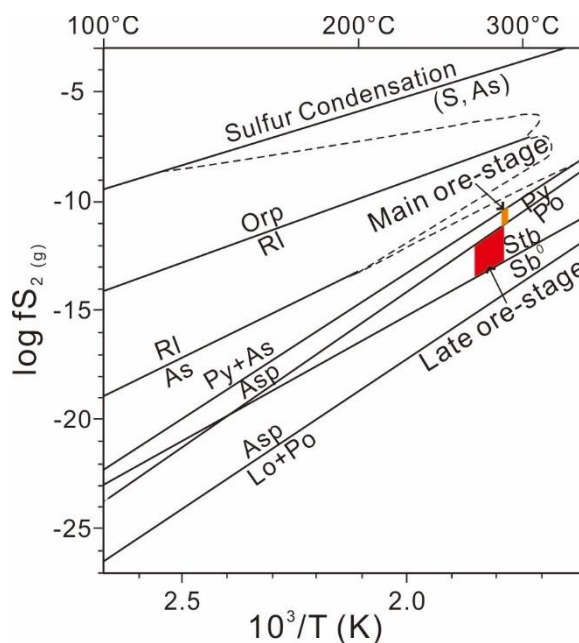


Figure 11. Temperature versus $\log f_{S_2(g)}$ diagram showing stability fields of minerals recorded in main and late-ore stages at the Yangshan gold belt [67]. Orange represents the stability field of main-ore stage pyrite and arsenopyrite, and red represents the stability field of late ore-stage stibnite. As-arsenic, Asp-arsenopyrite, Lo-loellingite, Orp-orpiment, Po-pyrrhotite, Py-pyrite, Rl-realgar, S-sulfur, Sb^0 -native antimony, Stb-stibnite.

7. Conclusions

The textural and geochemical characteristics of sulfides indicate multiple pulses of evolving hydrothermal fluids, with As becoming more abundant and S species less abundant with time until cessation of the main ore-stage. Arsenian pyrite was the dominant host for invisible gold until arsenopyrite became a common ore mineral and became the main host for invisible gold. Only once both pyrite and arsenopyrite ceased to be deposited did free gold become the dominant gold phase. There is thus a strong correlation between the relative activities of S and As and their total abundances in the ore fluid and the siting of gold in the Yangshan gold ores. Mass balance calculations indicate that there is no necessity to invoke remobilization processes to explain the occurrence of either invisible or visible gold in the ores. The only exception is for the Py_{1-2} replacement of Py_{1m} , where fluid-mediated coupled dissolution-precipitation reactions may have occurred to exchange Au between the two pyrite phases.

Supplementary Materials: The following are available online at <http://www.mdpi.com/2075-163X/9/2/92/s1>, Table S1: LA-ICP-MS elemental data for pyrite in typical gold deposits from Yangshan gold belt (in parts per million); Table S2: Correlation coefficient matrix diagram of trace-element contents of pyrite in this study.

Author Contributions: N.L. and J.D. conceived this contribution; N.L. and R.H. prepared the experiments; N.L. performed the experiments and wrote the original draft; N.L. and D.I.G. reviewed and edited the draft, with D.I.G. making several significant additions to interpretations.

Funding: This study was financially supported by the National Natural Science Foundation of China (Grant No. 41702072); the National Basic Research Program of China (Grant No. 2015CB452605); the Public Welfare Scientific Research Funding of China (Grant No. 201411048); the Geological investigation work project of the China Geological Survey (Grant No. 12120114038301); 111 Project of the Ministry of Education, China (Grant No. B07011); and the MOST Special Fund from the State Key Laboratory of Geological Processes and Mineral Resources, China University of Geosciences (Grant No. MSFGPMR201804).

Acknowledgments: We are grateful to Liqiang Yang, who made constructive comments on the manuscript. We would like to thank Xingzhong Ji, Zhichao Zhang, and Yuchen Zhao from China University of Geosciences, Beijing, for their assistance with field work. We are grateful for constructive comments by the reviewers.

Conflicts of Interest: The authors declare no conflict of interest.

References

1. Pitcairn, I.K.; Olivo, G.R.; Teagle, D.A.H.; Craw, D. Sulfide evolution during prograde metamorphism of the Otago and Alpine schists, New Zealand. *Can. Mineral.* **2010**, *48*, 1267–1295. [[CrossRef](#)]
2. Yang, L.Q.; Deng, J.; Wang, Z.L.; Guo, L.N.; Li, R.H.; Groves, D.I.; Danyushevsky, L.V.; Zhang, C.; Zheng, X.L.; Zhao, H. Relationships between gold and pyrite at the Xincheng gold deposit, Jiaodong Peninsula, China: Implications for gold source and deposition in a brittle epizonal environment. *Econ. Geol.* **2016**, *111*, 105–126. [[CrossRef](#)]
3. Cook, N.J.; Chryssoulis, S.L. Concentrations of invisible gold in the common sulfides. *Can. Mineral.* **1990**, *28*, 1–16.
4. Deng, J.; Wang, Q.F.; Li, G.J.; Zhao, Y. Structural control and genesis of the Oligocene Zhenyuan orogenic gold deposit, SW China. *Ore Geol. Rev.* **2015**, *65 Pt 1*, 42–54. [[CrossRef](#)]
5. Groves, D.I.; Goldfarb, R.J.; Robert, F.; Hart, C.J. Gold deposits in metamorphic belts: Overview of current understanding, outstanding problems, future research, and exploration significance. *Econ. Geol.* **2003**, *98*, 1–29.
6. Groves, D.I.; Santosh, M. The giant Jiaodong gold province: The key to a unified model for orogenic gold deposits? *Geosci. Front.* **2016**, *7*, 409–417. [[CrossRef](#)]
7. Velásquez, G.; Béziat, D.; Salvi, S.; Siebenaller, L.; Borisova, A.Y.; Pokrovski, G.S.; De Parseval, P. Formation and deformation of pyrite and implications for gold mineralization in the El Callao district, Venezuela. *Econ. Geol.* **2014**, *109*, 457–486. [[CrossRef](#)]
8. Yang, L.Q.; Deng, J.; Goldfarb, R.J.; Zhang, J.; Gao, B.F.; Wang, Z.L. ⁴⁰Ar/³⁹Ar geochronological constraints on the formation of the Dayingezhuang gold deposit: New implications for timing and duration of hydrothermal activity in the Jiaodong gold province, China. *Gondwana Res.* **2014**, *25*, 1469–1483. [[CrossRef](#)]
9. Deng, J.; Liu, X.F.; Wang, Q.F.; Pan, R.G. Origin of the Jiaodong-type Xinli gold deposit, Jiaodong Peninsula, China: Constraints from fluid inclusion and C–D–O–S–Sr isotope compositions. *Ore Geol. Rev.* **2015**, *65 Pt 3*, 674–686. [[CrossRef](#)]
10. Yang, L.Q.; Deng, J.; Guo, L.N.; Wang, Z.L.; Li, X.Z.; Li, J.L. Origin and evolution of ore fluid, and gold-deposition processes at the giant Taishang gold deposit, Jiaodong Peninsula, eastern China. *Ore Geol. Rev.* **2016**, *72*, 585–602. [[CrossRef](#)]
11. Yang, L.Q.; Guo, L.N.; Wang, Z.L.; Zhao, R.X.; Song, M.C.; Zheng, X.L. Timing and mechanism of gold mineralization at the Wang’ershan gold deposit, Jiaodong Peninsula, eastern China. *Ore Geol. Rev.* **2017**, *88*, 491–510. [[CrossRef](#)]
12. Deng, J.; Wang, C.M.; Bagas, L.; Carranza, E.J.M.; Lu, Y.J. Cretaceous–Cenozoic tectonic history of the Jiaojia Fault and gold mineralization in the Jiaodong Peninsula, China: Constraints from zircon U–Pb, illite K–Ar, and apatite fission track thermochronometry. *Miner. Depos.* **2015**, *50*, 987–1006. [[CrossRef](#)]
13. Mumin, A.H.; Fleet, M.E.; Chryssoulis, S.L. Gold mineralization in As-rich mesothermal gold ores of the Bogosu-Prestea mining district of the Ashanti Gold Belt, Ghana: Remobilization of “invisible” gold. *Miner. Depos.* **1994**, *29*, 445–460. [[CrossRef](#)]
14. Morey, A.A.; Tomkins, A.G.; Bierlein, F.P.; Weinberg, R.F.; Davidson, G.J. Bimodal Distribution of Gold in Pyrite and Arsenopyrite: Examples from the Archean Boorara and Bardoc Shear Systems, Yilgarn Craton, Western Australia. *Econ. Geol.* **2008**, *103*, 599–614. [[CrossRef](#)]
15. Lu, H.Z.; Zhu, X.Q.; Shan, Q.; Wang, Z.G. Hydrothermal evolution of gold-bearing pyrite and arsenopyrite from different types of gold deposits. *Miner. Depos.* **2013**, *32*, 823–842, (In Chinese with English Abstract).
16. Goldfarb, R.; Baker, T.; Dube, B.; Groves, D.I.; Hart, C.J.R.; Gosselin, P. Distribution, character and genesis of gold deposits in metamorphic terranes. In *Economic Geology 100th Anniversary*; Hedenquist, J., Thompson, J., Goldfarb, R.J., Eds.; Society of Economic Geologists: Littleton, CO, USA, 2005; pp. 407–450.
17. Sung, Y.-H.; Brugger, J.; Ciobanu, C.L.; Pring, A.; Skinner, W.; Nugus, M. Invisible gold in arsenian pyrite and arsenopyrite from a multistage Archean gold deposit: Sunrise Dam, Eastern Goldfields Province, Western Australia. *Miner. Depos.* **2009**, *44*, 765–791. [[CrossRef](#)]
18. Deol, S.; Deb, M.; Large, R.R.; Gilbert, S. LA-ICPMS and EPMA studies of pyrite, arsenopyrite and loellingite from the Bhukia-Jagpura gold prospect, southern Rajasthan, India: Implications for ore genesis and gold remobilization. *Chem. Geol.* **2012**, *326–327*, 72–87. [[CrossRef](#)]

19. Li, W.; Cook, N.J.; Xie, G.-Q.; Mao, J.-W.; Ciobanu, C.L.; Li, J.-W.; Zhang, Z.-Y. Textures and trace element signatures of pyrite and arsenopyrite from the Gutaishan Au–Sb deposit, South China. *Miner. Depos.* **2018**. [[CrossRef](#)]
20. Fougereuse, D.; Micklethwaite, S.; Tomkins, A.G.; Mei, Y.; Kilburn, M.; Guagliardo, P.; Fisher, L.A.; Halfpenny, A.; Gee, M.; Paterson, D.; et al. Gold remobilisation and formation of high grade ore shoots driven by dissolution-reprecipitation replacement and Ni substitution into auriferous arsenopyrite. *Geochim. Cosmochim. Acta* **2016**, *178*, 143–159. [[CrossRef](#)]
21. Reich, M.; Kesler, S.E.; Utsunomiya, S.; Palenik, C.S.; Chryssoulis, S.L.; Ewing, R.C. Solubility of gold in arsenian pyrite. *Geochim. Cosmochim. Acta* **2005**, *69*, 2781–2796. [[CrossRef](#)]
22. Pitcairn, I.K.; Skelton, A.D.L.; Wohlgemuth-Ueberwasser, C.C. Mobility of gold during metamorphism of the Dalradian in Scotland. *Lithos* **2015**, *233*, 69–88. [[CrossRef](#)]
23. Large, R.R.; Danyushevsky, L.; Hollit, C.; Maslennikov, V.; Meffre, S.; Gilbert, S.; Bull, S.; Scott, R.; Emsbo, P.; Thomas, H.; et al. Gold and trace element zonation in pyrite using a laser imaging technique: Implications for the timing of gold in orogenic and Carlin-style sediment-hosted deposits. *Econ. Geol.* **2009**, *104*, 635–668. [[CrossRef](#)]
24. Cook, N.J.; Ciobanu, C.L.; Meria, D.; Silcock, D.; Wade, B. Arsenopyrite-pyrite association in an orogenic gold ore: Tracing mineralization history from textures and trace elements. *Econ. Geol.* **2013**, *108*, 1273–1283. [[CrossRef](#)]
25. Deng, J.; Wang, Q.; Li, G.; Hou, Z.; Jiang, C.; Danyushevsky, L. Geology and genesis of the giant Beiya porphyry–skarn gold deposit, northwestern Yangtze Block, China. *Ore Geol. Rev.* **2015**, *70*, 457–485. [[CrossRef](#)]
26. Large, R.R.; Maslennikov, V.V.; Robert, F.; Danyushevsky, L.V.; Chang, Z.S. Multistage sedimentary and metamorphic origin of pyrite and gold in the giant Sukhoi Log deposit, Lena gold province, Russia. *Econ. Geol.* **2007**, *102*, 1233–1267. [[CrossRef](#)]
27. Large, R.R.; Bull, S.W.; Maslennikov, V.V. A carbonaceous sedimentary source-rock model for Carlin-type and orogenic gold deposits. *Econ. Geol.* **2011**, *106*, 331–358. [[CrossRef](#)]
28. Thomas, H.V.; Large, R.R.; Bull, S.W.; Maslennikov, V.; Berry, R.F.; Fraser, R.; Froud, S.; Moye, R. Pyrite and pyrrhotite textures and composition in sediments, laminated quartz veins, and reefs at Bendigo gold mine, Australia: Insights for ore genesis. *Econ. Geol.* **2011**, *106*, 1–31. [[CrossRef](#)]
29. Steadman, J.A.; Large, R.R. Synsedimentary, diagenetic, and metamorphic pyrite, pyrrhotite, and marcasite at the Homestake BIF-hosted gold deposit, South Dakota, USA: Insights on Au-As ore genesis from textural and LA-ICP-MS trace element studies. *Econ. Geol.* **2016**, *111*, 1731–1752. [[CrossRef](#)]
30. Gao, S.; Huang, F.; Gu, X.; Chen, Z.; Xing, M.; Li, Y. Research on the growth orientation of pyrite grains in the colloform textures in Baiyunpu Pb–Zn polymetallic deposit, Hunan, China. *Mineral. Petrol.* **2017**, *111*, 69–79. [[CrossRef](#)]
31. Dubosq, R.; Lawley, C.J.M.; Rogowitz, A.; Schneider, D.A.; Jackson, S. Pyrite deformation and connections to gold mobility: Insight from micro-structural analysis and trace element mapping. *Lithos* **2018**, *310–311*, 86–104. [[CrossRef](#)]
32. Li, X.-H.; Fan, H.-R.; Yang, K.-F.; Hollings, P.; Liu, X.; Hu, F.-F.; Cai, Y.-C. Pyrite textures and compositions from the Zhuangzi Au deposit, southeastern North China Craton: Implication for ore-forming processes. *Contrib. Mineral. Petrol.* **2018**, *173*, 73. [[CrossRef](#)]
33. Goldfarb, R.J.; Taylor, R.D.; Collins, G.S.; Goryachev, N.A.; Orlandini, O.F. Phanerozoic continental growth and gold metallogeny of Asia. *Gondwana Res.* **2014**, *25*, 48–102. [[CrossRef](#)]
34. Deng, J.; Wang, Q.F. Gold mineralization in China: Metallogenic provinces, deposit types and tectonic framework. *Gondwana Res.* **2016**, *36*, 219–274. [[CrossRef](#)]
35. Groves, D.I.; Goldfarb, R.J.; Gebre-Mariam, M.; Hagemann, S.G.; Robert, F. Orogenic gold deposits: A proposed classification in the context of their crustal distribution and relationship to other gold deposit types. *Ore Geol. Rev.* **1998**, *13*, 7–27. [[CrossRef](#)]
36. Li, N.; Deng, J.; Yang, L.Q.; Goldfarb, R.J.; Zhang, C.; Marsh, E.; Lei, S.B.; Koenig, A.; Lowers, H. Paragenesis and geochemistry of ore minerals in the epizonal gold deposits of the Yangshan gold belt, West Qinling, China. *Miner. Depos.* **2014**, *49*, 427–449. [[CrossRef](#)]

37. Li, N.; Deng, J.; Yang, L.-Q.; Groves, D.I.; Liu, X.-W.; Dai, W.-G. Constraints on depositional conditions and ore-fluid source for orogenic gold districts in the West Qinling Orogen, China: Implications from sulfide assemblages and their trace-element geochemistry. *Ore Geol. Rev.* **2018**, *102*, 204–219. [[CrossRef](#)]
38. Zhang, G.W.; Meng, Q.R.; Lai, S.C. Tectonics and structure of Qinling orogenic belt. *Sci. China Ser. B* **1995**, *38*, 1379–1394.
39. Meng, Q.R.; Zhang, G.W. Timing of collision of the North and South China blocks: Controversy and reconciliation. *Geology* **1999**, *27*, 123. [[CrossRef](#)]
40. Dong, Y.P.; Zhang, X.N.; Liu, X.M.; Li, W.; Chen, Q.; Zhang, G.W.; Zhang, H.F.; Yang, Z.; Sun, S.S.; Zhang, F.F. Propagation tectonics and multiple accretionary processes of the Qinling Orogen. *J. Asian Earth Sci.* **2015**, *104*, 84–98. [[CrossRef](#)]
41. Deng, J.; Wang, Q.F.; Li, G.J. Tectonic evolution, superimposed orogeny, and composite metallogenic system in China. *Gondwana Res.* **2017**, *50*, 216–266. [[CrossRef](#)]
42. Yan, Q.; Wang, Z.; Yan, Z.; Hanson, A.D.; Druschke, P.A.; Liu, D.; Song, B.; Jian, P.; Wang, T. Geochronology of the Bikou Group volcanic rocks: Newest results from SHRIMP zircon U-Pb dating. *Geol. Bull. China* **2003**, *22*, 456–458.
43. Chen, Y.J.; Zhang, J.; Zhang, F.; Franco, P.; Li, C. Carlin and Carlin-like gold deposits in Western Qinling Mountains and their metallogenic time, tectonic setting and model. *Geol. Rev.* **2004**, *50*, 134–152, (In Chinese with English Abstract).
44. Yang, L.Q.; Ji, X.Z.; Santosh, M.; Li, N.; Zhang, Z.C.; Yu, J.Y. Detrital zircon U-Pb ages, Hf isotope, and geochemistry of Devonian chert from the Mianlue suture: Implications for tectonic evolution of the Qinling orogen. *J. Asian Earth Sci.* **2015**, *113 Pt 2*, 589–609. [[CrossRef](#)]
45. Yang, L.Q.; Deng, J.; Qiu, K.F.; Ji, X.Z.; Santosh, M.; Song, K.R.; Song, Y.H.; Geng, J.Z.; Zhang, C.; Hua, B. Magma mixing and crust-mantle interaction in the Triassic monzogranites of Bikou Terrane, central China: Constraints from petrology, geochemistry, and zircon U-Pb-Hf isotopic systematics. *J. Asian Earth Sci.* **2015**, *98*, 320–341. [[CrossRef](#)]
46. Yang, L.Q.; Deng, J.; Dilek, Y.; Qiu, K.F.; Ji, X.Z.; Li, N.; Taylor, R.D.; Yu, J.Y. Structure, geochronology, and petrogenesis of the Late Triassic Puziba granitoid dikes in the Mianlue suture zone, Qinling orogen, China. *Geol. Soc. Am. Bull.* **2015**, *127*, 1831–1854. [[CrossRef](#)]
47. Dong, Y.P.; Zhang, G.W.; Neubauer, F.; Liu, X.M.; Genser, J.; Hauzenberger, C. Tectonic evolution of the Qinling orogen, China: Review and synthesis. *J. Asian Earth Sci.* **2011**, *41*, 213–237. [[CrossRef](#)]
48. Wang, X.X.; Wang, T.; Zhang, C.L. Neoproterozoic, Paleozoic, and Mesozoic granitoid magmatism in the Qinling Orogen, China: Constraints on orogenic process. *J. Asian Earth Sci.* **2013**, *72*, 129–151. [[CrossRef](#)]
49. Li, N.; Chen, Y.J.; Santosh, M.; Pirajno, F. Compositional polarity of Triassic granitoids in the Qinling Orogen, China: Implication for termination of the northernmost paleo-Tethys. *Gondwana Res.* **2015**, *27*, 244–257. [[CrossRef](#)]
50. Li, N.; Yang, L.Q.; Zhang, C.; Zhang, J.; Lei, S.B.; Wang, H.T.; Wang, H.W.; Gao, X. Sulfur isotope characteristics of the Yangshan gold belt, West Qinling: Constraints on ore-forming environment and material source. *Acta Petrol. Sin.* **2012**, *28*, 1577–1587, (In Chinese with English Abstract).
51. Li, N. Geochemistry of Ore-Forming Processes in the Yangshan Gold Belt, West Qinling, Central China. Ph.D. Thesis, China University of Geosciences, Beijing, China, 2013. (In Chinese with English Abstract).
52. Li, N.; Zhang, Z.C.; Liu, X.W.; Liu, J. The relationship between disseminated gold mineralization and vein-type gold-antimony mineralization: Example from the Yangshan gold belt, West Qinling. *Acta Petrol. Sin.* **2018**, *34*, 1312–1326, (In Chinese with English Abstract).
53. Zhao, H.X.; Frimmel, H.E.; Jiang, S.Y.; Dai, B.Z. LA-ICP-MS trace element analysis of pyrite from the Xiaoqinling gold district, China: Implications for ore genesis. *Ore Geol. Rev.* **2011**, *43*, 142–153. [[CrossRef](#)]
54. Longerich, H.P.; Jackson, S.E.; Günther, D. Inter-laboratory note. Laser ablation inductively coupled plasma mass spectrometric transient signal data acquisition and analyte concentration calculation. *J. Anal. At. Spectrom.* **1996**, *11*, 899–904. [[CrossRef](#)]
55. Zhao, J.; Liang, J.L.; Ni, S.J.; Xiang, Q.R. In situ sulfur isotopic composition analysis of Au-bearing pyrites by using Nano-SIMS in Yangshan gold deposit, Gansu Province. *Miner. Depos.* **2016**, *35*, 653–662, (In Chinese with English Abstract).
56. Ward, J.; Mavrogenes, J.; Murray, A.; Holden, P. Trace element and sulfur isotopic evidence for redox changes during formation of the Wallaby Gold Deposit, Western Australia. *Ore Geol. Rev.* **2017**, *82*, 31–48. [[CrossRef](#)]

57. Zhang, J.; Deng, J.; Chen, H.Y.; Yang, L.Q.; Cooke, D.; Danyushevsky, L.; Gong, Q.J. LA-ICP-MS trace element analysis of pyrite from the Chang'an gold deposit, Sanjiang region, China: Implication for ore-forming process. *Gondwana Res.* **2014**, *26*, 557–575. [[CrossRef](#)]
58. Yang, L.Q.; Deng, J.; Li, N.; Zhang, C.; Ji, X.Z.; Yu, J.Y. Isotopic characteristics of gold deposits in the Yangshan gold belt, West Qinling, central China: Implications for fluid and metal sources and ore genesis. *J. Geochem. Explor.* **2016**, *168*, 103–118. [[CrossRef](#)]
59. Cook, N.J.; Ciobanu, C.L.; Mao, J.W. Textural control on gold distribution in As-free pyrite from the Dongping, Huangtuliang and Hougou gold deposits, North China Craton (Hebei Province, China). *Chem. Geol.* **2009**, *264*, 101–121. [[CrossRef](#)]
60. Li, Z.-K.; Li, J.-W.; Cooke, D.R.; Danyushevsky, L.; Zhang, L.; O'Brien, H.; Lahaye, Y.; Zhang, W.; Xu, H.-J. Textures, trace elements, and Pb isotopes of sulfides from the Haopinggou vein deposit, southern North China Craton: Implications for discrete Au and Ag–Pb–Zn mineralization. *Contrib. Mineral. Petrol.* **2016**, *171*, 99. [[CrossRef](#)]
61. Yue, H. *Flotation Test of Primary Ore from Yangshan Gold Deposit*; Changchun Gold Research Institute: Changchun, China, 2011; pp. 1–145, (In Chinese with English Abstract).
62. Yan, F.Z.; Qi, J.Z.; Guo, J.H. *Geology and Exploration of Yangshan Gold Deposit in Gansu Province*; Geological Publishing House: Beijing, China, 2010; p. 236.
63. Liang, J.L.; Sun, W.D.; Zhu, S.Y.; Li, H.; Liu, Y.L.; Zhai, W. Mineralogical study of sediment-hosted gold deposits in the Yangshan ore field, Western Qinling Orogen, Central China. *J. Asian Earth Sci.* **2014**, *85*, 40–50. [[CrossRef](#)]
64. Williams-Jones, A.E.; Norman, C. Controls of mineral parageneses in the system Fe-Sb-S-O. *Econ. Geol.* **1997**, *92*, 308–324. [[CrossRef](#)]
65. An, F.; Zhu, Y. Native antimony in the Baogutu gold deposit (west Junggar, NW China): Its occurrence and origin. *Ore Geol. Rev.* **2010**, *37*, 214–223. [[CrossRef](#)]
66. Xie, Z.J.; Xia, Y.; Cline, J.S.; Yan, B.W.; Wang, Z.P.; Tan, Q.P.; Wei, D.T. Comparison of the native antimony-bearing Paiting gold deposit, Guizhou Province, China, with Carlin-type gold deposits, Nevada, USA. *Miner. Depos.* **2017**, *52*, 69–84. [[CrossRef](#)]
67. Simon, G.; Kesler, S.E.; Chryssoulis, S. Geochemistry and textures of gold-bearing arsenian pyrite, Twin Creeks, Nevada; implications for deposition of gold in carlin-type deposits. *Econ. Geol.* **1999**, *94*, 405–421. [[CrossRef](#)]



© 2019 by the authors. Licensee MDPI, Basel, Switzerland. This article is an open access article distributed under the terms and conditions of the Creative Commons Attribution (CC BY) license (<http://creativecommons.org/licenses/by/4.0/>).